Numerical Simulation of MZF Design with Non-planar Hydraulic Fracturing from Multi-lateral Horizontal Wells

B. Sobhaniaragh[a,b,*], J. Trevelyan[c], W.J. Mansur[a,b], F.C. Peters[a,b]

[a]*Laboratório de Métodos de Modelagem e Geofísica Computacional (LAMEMO), Federal University of Rio de Janeiro, 21941-596, RJ, Brazil*
[b]*Department of Civil Engineering, COPPE, Federal University of Rio de Janeiro, RJ, Brazil*
[c]*School of Engineering and Computing Sciences, Durham University, South Road, Durham DH1 3LE, United Kingdom*

Abstract

In recent years, developments in the oil and gas industry have evolved significantly in advancing the mechanical systems technology to perform hydraulic fracturing. However, further developments will require an in-depth understanding of the impacts of fracture spacing, stress anisotropy, and reservoir characterization. In order to develop a comprehensive and robust completion design for hydraulic fracturing from multi-lateral wellbores with closely spaced fractures, it is important to consider stress shadowing effects. In this work the Cohesive Segments Method is combined with the Phantom Node Method, a combination termed CPNM. This is capable of not only simulating non-planar hydraulic fracture propagation with an unpredictable path, but also simulating the emergence of multiple cohesive cracks within a porous medium. This paper focuses on the "Modified Zipper-Frac" (MZF) design, which has been introduced to design the clusters from multi-lateral wells with the aim of increasing the fracture complexity. Validation of the numerical technique has been performed by comparing the solution for an individual hydraulic fracture with a Khristianovic-Geertsma-de Klerk (KGD) solution. In addition, a study of the development of double fractures has been conducted in the presence of stress shadowing to verify the simulation results. Taking the stress shadowing effects into account, a large number of numerical simulations are conducted using CPNM to investigate the stress anisotropy as well as the in-plane shear stress in the area between the two wells. The main contribution of this work is the detailed investigation of the effects of stress shadowing as a function of the fracture spacing on the horizontal stress contrast, direction of maximum local stress, leak-off flow rate, in-plane shear stress, and pore pressure of the formation.

Keywords: Hydraulic fracturing, Modified zipper-frac design, Non-planar crack propagation, Stress shadow effect, Cohesive phantom node method.

1. Introduction

The revolution of unconventional reservoirs, particularly shale plays, is altering the worldwide energy market, contributing to the downward pressure on gas prices across the globe and the forthcoming independence of the United States on natural gas imports. From 2008 to 2014, production of crude oil and natural gas rocketed from 6.78 Million Barrels Per Day (MMBD) to 8.91 MMBD; this was mainly due to horizontal wells as well as hydraulic fracturing in shale and tight formations which were previously inaccessible (Stevens, 2012; Winegarden, 2016). Apart from

*Corresponding author
Email address: behnam.sobhaniaragh@durham.ac.uk, sobhaniaragh@coc.ufrj.br (B. Sobhaniaragh)

horizontal drilling, Hydraulic Fracturing (HF) technology, a well stimulation technique which involves injecting large volumes of a fracturing fluid at high pressure into the well to fracture the rock formation, has played a pivotal role in exploiting shale reservoirs.

Recent estimations obtained from well-testing analysis during the early production life of wells in shale formations have concluded that the fracture surface area is far larger than in conventional HF design or the estimated regions confined by the scattering domain of micro-seismic events. This stems from the fact that vast majority of tight sand and shale formations are naturally fractured, so that these reservoirs consist of planes of weakness irregularly distributed in the reservoir. A complex fracture network therefore develops, including induced hydraulic fractures as well as primary and secondary natural fractures. A number of attempts (Meyer et al., 2011; Nagel et al., 2011) have been made to explain the far-field fracture networks and their consequences on the propagation of induced fractures. However, the acquisition of fundamental data on pre-existing networks presents considerable challenges. Wu and Pollard (2002) and Olsen et al. (2009) demonstrated that the width at the intersection of a hydraulically induced fracture and a natural fracture is dependent on several parameters such as the stress anisotropy. A reduction in stress anisotropy can activate Mode I opening at planes of weakness, leading to the generation of a complex network which links hydraulically induced fractures to pre-existing natural fractures. Hence, the presence of a large fracture surface area causes higher drainage of the low permeability reservoir and maximizes the Stimulated Reservoirs Volume (SRV). Weng et al. (2007) showed that the hydraulic fracture geometry changes from a bi-wing fracture to a complex network of fractures as a result of a reduction in the difference in horizontal stresses.

Various completion techniques on an individual horizontal wellbore have been employed to generate the complex network and thereby enhance the total SRV. Simultaneously HF (Sim-HF) and sequentially HF (Seq-HF) are among the most widely used stimulation techniques in shale reservoirs. Recently, a new strategy termed "Texas two-step" has been introduced to reduce the Fracture Spacing (FS) and promote greater fracture complexity. According to this technique, after fluid injection into the first interval, by moving towards the heel, a second interval is stimulated and, as a result, there is a degree of stress interference between the two fractures. Afterwards, rather than continuing towards the heel of the well, a third interval is stimulated between the two previously fractured intervals with the aim of altering the stress in the rock so as to contribute to the generation of secondary fractures. Using a finite difference and explicit numerical scheme, Roussel et al. (2011) and Manchanda et al. (2014) showed that a lower FS can be achieved in Texas two-step compared with Sim-HF. In addition, they proposed that a stress reversal region with a stress re-orientation of 90° takes place in the material adjacent to the main induced fracture. This zone imposes a constraint on the FS that it should be sufficiently large to avoid the initiation of longitudinal fractures. However, this hypothesis seems to be questionable because the propagation of a new fracture into a region in which the stress has been altered by a previous fracture can cause significant changes in the local stresses. This results in two distinct regions, including repulsion and attraction zones; these will be discussed in the present paper.

As far as HF from multi-wells is concerned, several techniques have been proposed to encourage far-field fracture complexity. "Zipper-Frac" is one of a class of techniques in which two or more horizontal wellbores are fractured simultaneously in order to enhance stress perturbation close to the tips of each fracture. In this method, when opposing fractures move towards each other, to some extent the interference takes place ahead of fracture and encourages the fractures to propagate through the direction perpendicular to the horizontal wellbore. However, the application of Zipper-Frac is restricted because of two main deficiencies. Firstly, the creation of complex field is limited to the area close to the fractures tips. Secondly, it is associated with the risk of connec-

tion of adjacent wellbores if opposing fractures become very close. Motivated by the advantages of the presence of a middle fracture between two consecutive fractures used in Texas two-step, another method, known as "Modified Zipper-Frac" (MZF) (Soliman et al., 2010), involves fractures from two lateral wells situated in a staggered pattern. Using the principles of continuum geomechanics, Rios et al. (2013) performed stress shadow analysis and proposed that Zipper-Frac creates an extensive region of increased normal stresses and decreased shear stresses. This has the effect of stabilizing natural fractures and weakness planes instead of enhancing the shear stress. Rafiee et al. (2012) studied the advantages of Zipper-Frac and the MZF approaches by using analytical stress interference calculations around various fracture geometries. They showed that the MZF completion potentially increases the stress interference between the fractures and provides greater fracture complexity than Zipper-Frac. However, this study did not consider the non-planar propagation of hydraulic fractures, an important effect when closely spaced fractures are used. By using the discrete element method, Nagel et al. (2013) showed that the improvement in well stimulation using the Zipper-Frac and MZF approaches is highly dependent upon the in-situ pore pressure, the natural fracture mechanical properties, and the natural fracture characteristics. Recently, Kumar and Ghassemi (2016) implemented a boundary element model with capabilities to simulate any number of fractures for Sim-HF and Seq-HF scenarios. Their results demonstrated that in Zipper-Frac, the fractures propagate with probability of coalescence of their tips. In the case of the MZF, the likelihood of fracture tips coalescing decreases because of the offset between fractures.

One of the leading factors in multiple HF design is the "stress shadow effect", which is a stress interference among multiple fractures in the vicinity of single or multi-wellbores. Gaining an in-depth understanding of this effect is seen as important for engineers seeking to mitigate risk and maximize the profitability of multiple fracturing treatments. Nonetheless, few studies have been carried out to investigate the impacts of stress shadowing on HF from individual or multi-lateral wellbores. The consequences of this effect on various completion procedures from multi-lateral wellbores in the upper Barnett shale have investigated by Vermylen et al. (2011) using microseismic events. Their results showed considerable discrepancies in completion outcomes owing to stress shadow effects. A numerical evaluation of the impacts of stress shadowing on multi-stage hydraulic fractures as a function of FS and the in-situ stress ratio has been conducted by Nagel et al. (2011), though this study neglected fluid leak-off. They found that with sequential fracturing, the second fracture, which grows under the stress shadow of an initial fracture, exhibits very little associated natural fracture shearing. Roussel et al. (2010) employed a 3-D numerical method of stress interference for simultaneously and sequentially fracturing approaches. They concluded from a series of numerical models that stress interference or reorientation increases with the number of fractures propagated and is dependent on the sequence of fracturing. Based on an enhanced 2-D displacement discontinuity method, Wu et al. (2012) investigated the stress shadowing effects in a complex hydraulic fracture network, showing that fractures can either enhance or repel each other depending on their initial spacing due to the impacts of stress shadowing.

In order to develop a comprehensive and robust completion design for HF from multi-lateral wellbores with closely spaced fractures, it is of great importance to contemplate stress shadowing effects. According to the authors' survey, most available works (Haddad and Sepehrnoori, 2015; Olson et al., 2009; Nagel et al., 2014), however, overlooked either the stress shadowing effects or the non-planar hydraulic fracture from multi-lateral wellbores owing to the restrictions on the numerical techniques adopted. In addition, very few works (Kumar and Ghassemi, 2016; Sesetty et al., 2015) have been dedicated to the MZF design. Inspired by the lack of an effective numerical tool in the available literature, the Cohesive Segments Method in combination with Phantom Node Method, termed CPNM (Sobhaniaragh et al., 2016b,a), has been established. The CPNM

is capable of not only simulating non-planar hydraulic fracture propagation along a path that is not predefined, but also of simulating the emergence of multiple cohesive cracks within a porous medium. The primary contributions of this study are to shed light on the effects of stress shadowing as a function of the FS on the horizontal stress contrast, direction of maximum horizontal stress, leak-off flow rate, in-plane shear stress, and pore pressure of the formation. By conducting a large number of numerical simulations, this paper is devoted to evaluating the stress anisotropy as well as shear stress to increase the probability of activating natural fractures, thereby increasing the fracture complexity and higher drainage area.

2. Fundamental Framework

Simulation of HF in a poro-elastic formation comprises the coupling of complex physical mechanisms including the following: deformation of the solid phase caused by the stress concentration owing to the fluid pressure on the fracture boundaries, fluid flow inside the porous medium enclosing the fracture, flow of the fracturing fluid through the crack, and infiltration of fracturing fluid into the poro-elastic formation, termed fluid leak-off. As sketched in Fig. 1, consider a hydraulic fracture propagating in a porous rock, which is assumed to be isotropic and poro-elastic. The material undergoes quasi-static deformation by injection of a viscous fluid from the wellbore into the perforation. Fig. 1 shows two different zones and crack tips. The first zone refers to the Fracture Process Zone (FPZ), which is described as the region around the crack tip where cohesive stresses apply across the crack. The other region is the broken cohesive zone, where the crack surfaces are traction free and the crack is filled with fracturing fluid. Based on the Cohesive Crack Model (CCM) (Needleman, 1987; Hillerborg, 1985), two different types of crack tip are identified, these being the "real crack tip" and the "fictitious crack tip"(Carpinteri, 2012; Hattori et al., 2017). The former implies the point delineating the stress-free area from the FPZ, whereas the latter is the point delineating the FPZ from the uncracked material. The ultimate stress is identical to a finite stress at the fictitious crack tip. As a result, any difficulty associated with a stress singularity is mitigated. In other words, the CCM overcomes the singularity of the stress field at the crack tip, a result of the more simplified Linear Elastic Fracture Mechanics (LEFM) theory. It is presupposed that the two-phase porous medium containing the fracture remains under isothermal conditions.

2.1. Fracturing Fluid Model

The primary task of fracturing fluids is to induce fractures to propagate through the formation. Continual pumping of fracturing fluid causes a conductive path to form and to extend deep into a formation in order to transmit a large volume of propping agent inside the induced fractures. Both Newtonian fluids, such as water, or non-Newtonian fluids, such as polymer solutions, are frequently used as HF fluids. Herein, for the sake of avoiding complex fluid behaviour, an incompressible and Newtonian fluid is considered. The flow model of the fluid within the fracture between the cohesive faces is depicted in Fig. 2. In this figure, the elements numbered 1 and 2 are fractured and element number 3 is intact. In the proposed model, the fluid flow through the fracture is decomposed into two components, i.e. the tangential flow along the cracked element faces and the normal flow across the cracked element surface. The normal component represents the infiltration mechanism into the surrounding formation. Based on lubrication theory, the momentum equation for the tangential fluid flow within the fracture is given by Poiseuille's law (Zimmerman and Bodvarsson, 1996)

$$q_t = -\frac{w^3}{12\mu}\frac{\partial p_F}{\partial s} \tag{1}$$

where w is the fracture aperture, μ is the dynamic viscosity of the fluid, q_t is the fracturing fluid flux of the tangential flow within the fracture surface, p_F is the pressure of the fluid through the fracture parameterized with the curvilinear coordinate, s.

The continuity equation of mass conservation for the fracturing fluid flow is described by (Zienkiewicz and Shiomi, 1984)

$$\frac{\partial w}{\partial t} + \frac{\partial q_t}{\partial s} + v_{top} + v_{bot} = 0 \tag{2}$$

where v_{top} and v_{bot} are the normal flow velocities at which the fracturing fluid leaks off from the top and bottom surfaces of the crack into the formation.

Most studies on the modelling of HF have assumed a 1-D fluid loss pattern into the formation in a direction perpendicular to the fracture plane, based on an explicit Carter's fluid flow model (Carter, 1957; Bunger et al., 2005). According to Carter's model, the fluid leak-off is expressed as an inverse square-root law of time of the form (Carter, 1957)

$$v_L = \frac{c_L}{\sqrt{t}} \tag{3}$$

where v_L denotes the leak-off velocity, c_L (having units $[\mathrm{LT}^{-1/2}]$) is the Carter's leak-off coefficient, and t is the time elapsed since the beginning of the infiltration procedure. In addition, Carter (Carter, 1957; Bunger et al., 2005) proposed that the volume of fluid leaked per unit area of the fracture, V_L, can be obtained from

$$V_L = 2c_L\sqrt{t} + S_p \tag{4}$$

where S_p is a spurt-loss coefficient, which is the volume of the fluid that percolates instantaneously before forming a filter cake. The deficiency of the Carter model, which is independent of fluid pressure of the filter cake, motivates this research to employ another approach. In this paper, in order to treat the filter cake as a pressure-dependent layer, Settari's fluid leak-off model (Settari et al., 1984) is employed by using a user-defined subroutine. By virtue of the proposed pressure-dependent model, the normal components of the fracturing fluid are defined as (Settari et al., 1984)

$$v_{top} = c_{top}\left(p_F - p_{top}\right) \tag{5}$$

$$v_{bot} = c_{bot}\left(p_F - p_{bot}\right) \tag{6}$$

where p_{top} and p_{bot} are the pore fluid pressures on the top and bottom faces of the crack, and c_{top} and c_{bot} are leak-off coefficients, which are pressure dependent and can be interpreted as the permeability of a filter cake built up on the walls of the fracture. The value of those coefficients depends on two factors (Adachi, 2001). One is the degree of the permeability of the porous formation. For example, in a matrix of low permeability, such as a tight sandstone or shale, the value of leak-off coefficients is very small, leading to a thicker filter cake. The other factor is the properties of the fracturing fluid. As some fracturing fluids, such as water-based high-molecular-weight polymer solutions, infiltrate into the surrounding formation, several of the dense polymers deposit on the walls of the fracture, forming a filter cake.

2.2. Coupled Fluid-Solid Equations

Based on theory of poro-elasticity (Terzaghi, 1951), the total stress at each point in the porous rock can be decomposed into the effective stress and pore pressure of the fluid phase. The former operates among the solid grains and governs their deformation and loading capacity. Hence, the relation between the total stress and effective stress is defined by (Terzaghi, 1951)

$$\boldsymbol{\sigma}' = \boldsymbol{\sigma} - \alpha p \mathbf{I} \tag{7}$$

in which $\boldsymbol{\sigma}'$ denotes the effective stress operating between solid grains, $\boldsymbol{\sigma}$ is the total Cauchy stress tensor, and p is the pore pressure, $\mathbf{I}$ is the second-order unit tensor. Parameter α is the Biot-Willis coefficient, which for isotropic materials can be given by $\alpha = 1 - K_T/K_S$, where K_T and K_S denote the bulk moduli of the porous material and the solid grains, respectively. In the absence of body forces, the equilibrium equation for the two-phase porous medium is described in the strong form as (Charlez, 1997)

$$\nabla.\boldsymbol{\sigma} = 0 \tag{8}$$

The continuity equation for the fluid flow within the porous rock, which equates the rate of increase of the fluid volume at a point to the rate of fluid volume flowing into the point during the time increment, is expressed as (Zienkiewicz and Shiomi, 1984; Zimmerman and Bodvarsson, 1996)

$$\frac{1}{Q}\dot{p} + \alpha\nabla.\dot{\mathbf{u}} + \nabla.\mathbf{v_f} = 0 \tag{9}$$

where $\mathbf{v_f}$ is the Darcy velocity vector of the pore fluid and Q is Biot's modulus, which describes the storage owing to the compressibility of the solid grains and fluid phase, related according to (Zienkiewicz and Shiomi, 1984)

$$\frac{1}{Q} = \frac{\varphi_0}{K_f} - \frac{\alpha - \varphi_0}{K_S}. \tag{10}$$

Here K_f denotes the bulk modulus of the pore fluid and φ_0 is the initial porosity. The Darcy relation for the pore fluid flow within the porous formation is given by (Khoei and Mohammadnejad, 2011)

$$\mathbf{v_f} = -\frac{\mathbf{k}}{\mu}\nabla p \tag{11}$$

where $\mathbf{k}$ is the permeability of the porous medium, which may take a scalar value k for the case of an isotropic medium. The term μ is the dynamic viscosity of the fluid. More details on the weak form of the governing equations and numerical technique are presented in Appendix A.

2.3. Cohesive Crack Model

In the considerable volume of literature on fracture mechanics in petroleum engineering, either empirical approaches or LEFM have been employed, leading to reasonable predictions in hard rock. Nonetheless, LEFM-based models provide conservative estimates in ductile shale or soft rocks such as weakly consolidated sandstone or clay. This arises from the role of non-linear fracture processes ahead of the crack, occurring within the FPZ, where the material softens moderately and energy dissipates on account of the development of micro-cracks.

In the present study, formulated by particular traction-separation laws, a CCM is proposed which is independent of the constitutive characteristics of the bulk material. By contrast with the

LEFM, in which the small FPZ is lumped into the crack tip, in the CCM the FPZ is aggregated into the crack surfaces. From a meso-scale standpoint, the micro-cracks are initiated at the interface of the matrix and aggregates, followed by the formation of a macro-crack through the coalescence of micro-cracks, as demonstrated in Fig. 1. The heterogeneous composition of geo-materials induces distinct phenomena such as crack bridging, which implies the connection of parallel cracks by virtue of an aggregate. This process accounts for the cohesive forces being carried by means of an existing fracture, and accordingly to facilitate modelling of the material with strain-softening characteristics Baker and Karihaloo (2004).

Contrary to the widely used intrinsic cohesive crack model (Camacho and Ortiz, 1996; Tvergaard and Hutchinson, 1992), which requires initial (penalty) stiffness, in the present paper an extrinsic model is employed, avoiding initial stiffness requirements. As a result, interface cohesive elements are embedded in the finite element model automatically only when the bulk material fulfils a specific criterion for crack initiation. The extrinsic CCM used in this work involves a linear, rate dependent traction-separation law which associates the displacement opening vector $\mathbf{\Delta}$ with the cohesive traction vector $\mathbf{T}$ applying across the cohesive faces. Vectors $\mathbf{\Delta}$ and $\mathbf{T}$ can be expressed with respect to their components as $\mathbf{\Delta} = \{\delta_n, \delta_s\}^T$ and $\mathbf{T} = \{T_n, T_s\}^T$ in two-dimensions for a mixed-mode formulation (Eq. 16). n designates the normal component and s denotes shear components. As illustrated in Fig. 3, we assume opening mode I and the maximum principal stress criterion for damage initiation. The FPZ undergoes broadening if the normal traction reaches the maximum value ${T_n}^0$, while the real crack tip displacement, i.e., opening is still zero. As the fracture opens, the cohesive stress reduces to zero, and finally the real crack tip displacement reaches a maximum value, ${\delta_n}^m$.

The failure mechanism consists of two critical consecutive components including a damage initiation criterion and a damage evolution law, as described in the following:

- Considering maximum nominal stress criterion (Ingraffea et al., 1977; Sih, 1973) as the damage initiation criterion, damage initiates when the maximum nominal stress ratio reaches a particular value. The proposed criterion is described by

$$fc = \max\left\{\frac{\langle T_n \rangle}{{T_n}^0}, \frac{T_s}{{T_s}^0}\right\} \tag{12}$$

  in which fc is a threshold parameter defining the fracture criterion, the symbol $\langle\rangle$ denotes the Macaulay bracket, and superscript 0 designates the damage initiation. Either a crack is initiated or the crack length of a pre-existing crack is extended when fc reaches the value of 1.0 according to a provided tolerance

$$1.0 \leq fc \leq (1.0 + fc_{tol}) \tag{13}$$

  Herein fc_{tol} is assumed to be 0.05.

- In order to deal with the damage evolution, two main components need to be introduced. Firstly, as depicted in Fig. 3, either the effective displacement at final failure, δ^m, or the fracture energy, G^c needs to be specified. Secondly, it is necessary to define the nature of the evolution of the damage parameter, D, between damage initiation and complete failure. The damage evolution law determines the rate at which the stiffness of the material degrades when the specific initiation criterion is fulfilled. The normal and shear traction components

are affected by the damage according to

$$T_n = \begin{cases} (1-D){T_n}^0, & {T_n}^0 \geq 0 \\ {T_n}^0, & {T_n}^0 < 0 \end{cases} \tag{14}$$

$$T_s = (1-D){T_s}^0 \tag{15}$$

where D is the scalar variable of the global damage, which varies from 0 to 1 upon more loading after the damage initiation.

In this paper, the Benzeggagh-Kenane (BK) model (Benzeggagh and Kenane, 1996) is implemented to determine the mixed-mode fracture propagation, and accordingly the fracture propagates when

$$G_{eq}^c = G_n^c + \left(G_s^c - G_t^c\right)\left(\frac{G_s}{G_n + G_s}\right)^\eta \tag{16}$$

in which G_{eq}^c is the equivalent critical energy release rate, the superscript c represents the energy release rate, and η refers to a material property which is taken here as 2.3 for the case of quasi-brittle material. Based on the BK model, the fracture initiates when the energy release rate approaches the value of G_{eq}^c.

Under mixed-mode fracture conditions, with a combination of normal and shear deformation, a damage evolution criterion can be written in terms of the effective displacement, as

$$\delta_{eq} = \sqrt{\langle\delta_n\rangle^2 + {\delta_s}^2} \tag{17}$$

It is worth noting that the area under the traction-separation law, as depicted in Fig. 3, is equal to the fracture energy, G^c, which is the energy dissipated per unit area of new developed crack surface.

2.4. Cohesive phantom node method

The CPNM has emerged as a highly appropriate numerical method in fracture mechanics. It allows the modelling of hydraulic fractures propagating along paths that do not need to be defined a priori. It also allows the emergence of multiple cohesive cracks with a FPZ ahead of the crack tip. The method is implemented into a finite element analysis package (Abaqus) along with user-defined subroutines. To model of fluid flow through the cracked element, extra phantom nodes relating to pore pressure degrees of freedom are added on the edges of enhanced elements. These phantom nodes are positioned on the original real nodes and allow for discontinuities in both displacement and fluid pressure to develop within a cracked element. The phantom nodes on the edges of each element are not activated unless the element is intersected by a crack and decohesion initiates. The crack propagation path is unrelated to the mesh. Thus the new cohesive segments, with activated phantom nodes, can nucleate at arbitrary locations with arbitrary orientations, and the existing ones are allowed to grow in an arbitrary direction when a critical condition is satisfied.

As illustrated in Fig. 2, let us consider a 2-D element (element number 1) with node numbers 1 to 4, which is intersected by a crack at Γ_c, separating the element domain into two sub-domains, Ω_A and Ω_B. Before they are activated, the phantom nodes, shown by white circles in Fig. 4, are positioned on the original nodes. After damage initiation, the phantom nodes are activated; each

phantom node and its corresponding real node are no longer tied together. The present element is subdivided into two sub-elements, i.e. element A and element B, which are formed by the node numbers 1 to 4 and $\tilde{1}$ to $\tilde{4}$. The elements do not share nodes and, as a result, represent an independent displacement field and pore pressure. The active part of element A is termed Ω_A and the active part of element B is named Ω_B. The formulation of the displacement field is described by (Rabczuk et al., 2008)

$$\mathbf{u}^A(\mathbf{x},t) = \mathbf{N}_j(\mathbf{x})\mathbf{u}_j^A(t), \qquad \mathbf{x} \in \Omega_A \tag{18}$$

$$\mathbf{u}^B(\mathbf{x},t) = \mathbf{N}_j(\mathbf{x})\mathbf{u}_j^B(t), \qquad \mathbf{x} \in \Omega_B, \tag{19}$$

and the displacement field approximation over $\Omega_A \cup \Omega_B$ becomes (Rabczuk et al., 2008)

$$\mathbf{u}(\mathbf{x},t) = \sum_{j\in n_A} \underbrace{\mathbf{N}_j^u(\mathbf{x})\mathbf{u}_j^A(t)}_{\mathbf{u}^A(\mathbf{x},t)} H(-\phi(\mathbf{x})) + \sum_{j\in n_B} \underbrace{\mathbf{N}_j^u(\mathbf{x})\mathbf{u}_j^B(t)}_{\mathbf{u}^B(\mathbf{x},t)} H(\phi(\mathbf{x})) \tag{20}$$

in which n_A and n_B are node sets of elements A and B, respectively; $\phi(\mathbf{x})$ is the signed distance measured from the crack, $H(\mathbf{x})$ is the Heaviside step function, and $\mathbf{N}_j^u$ is the standard finite element shape function of node j. This formulation is associated with the form proposed by Hansbo and Hansbo (2004). It was demonstrated by Areias and Belytschko (2005) that the formulation of Hansbo and Hansbo is another form of the XFEM displacement field. The pore fluid pressure $p(\mathbf{x},t)$ is approximated in an analogous manner as

$$p(\mathbf{x},t) = \sum_{j\in n_A} \underbrace{\mathbf{N}_j^p(\mathbf{x})p_j^A(t)}_{p^A(\mathbf{x},t)} H(-\phi(\mathbf{x})) + \sum_{j\in n_B} \underbrace{\mathbf{N}_j^p(\mathbf{x})p_j^B(t)}_{p^B(\mathbf{x},t)} H(\phi(\mathbf{x})) \tag{21}$$

where p_j^A denotes the standard pressure degrees of freedom for the node j relating to the element A, and $\mathbf{N}_j^p$ is the standard finite element shape function of node j.

As no adjustment of the mesh around the crack geometry is required, it becomes useful to make use of techniques to track moving interfaces. One effective technique is the level set method (Sethian, 1999). Here, the interface of interest is described by the zero level set of a function which is one dimension higher than that of the interface. The evolution equation for the interface can then be designated as an equation for the evolution of level set function. Suppose a domain Ω is partitioned into two sub-domains Ω_1 and Ω_2, as shown in Fig. 4. The interface between these two sub-domains is denoted by Γ_d. The signed distance function, as the most common level set function, is characterized for the representation of the crack geometry as

$$\phi(\mathbf{x}) = \left\|\mathbf{x} - \mathbf{x}^*\right\| \operatorname{sign}\left(\mathbf{n}_{\Gamma_d}.\left(\mathbf{x} - \mathbf{x}^*\right)\right) \tag{22}$$

where $\mathbf{x}^*$ refers to the nearest point projection of $\mathbf{x}$ onto the crack Γ_d, and $\mathbf{n}_{\Gamma_d}$ denotes the normal vector to the crack surface at point $\mathbf{x}^*$. According to this definition, $\|\,\|$ denotes the Euclidean norm, where $\|\mathbf{x} - \mathbf{x}^*\|$ is the distance of point $\mathbf{x}$ to the crack surface Γ_d. To model the crack propagation problem, just one level set ϕ is not normally adequate to capture the crack geometry, and another level set ψ at the crack tip is required. Therefore, the crack geometry is defined by two, almost orthogonal, signed distance functions. The first, ϕ, is used for the crack surface, while the second, ψ, is used to establish an orthogonal surface so that the intersection of the two surfaces locates the

crack tip.

3. Construction of Computational Model

Fig. 5 represents a three-dimensional configuration of two horizontal wellbores. The trajectories of the horizontal wells are aligned with the minimum horizontal stress, resulting in transverse fractures. The computational finite element domain, demonstrated in Fig. 6, for HF initiation and propagation simulation is a 2-D horizontal plane (i.e. the out-of-plane stress is vertical) which includes two horizontal wellbores, and perforation holes. The area ABCD, which is the main domain of hydraulically induced crack propagation, discretized with a fine mesh, has a length of 510 m and a width of 100 m. The mesh refinement is gradually decreased through mesh transition. The whole domain is considered large enough to eliminate the consequences of geometrical and pore pressure boundary conditions. The model is discretized as a fully saturated porous domain with CPE4RP elements (4-node bilinear displacement and pore pressure, reduced integration with hourglass control) together with enhanced hourglass control (Belytschko et al., 1984) to remedy the problem of instabilities. For the computational model depicted in Fig. 6, the maximum mesh size in the area ABCD should be 0.4 m to achieve the convergence in the results obtained. The horizontal wellbores No. 1 and No. 2 are located in the plane of the horizontal stresses, $S_{h,\min}$ and $S_{H,\max}$, at the upper and lower sides of the computational domain. The fully coupled pore pressure-stress analysis consists of the following steps. The first step (named the *geostatic step*) is initially carried out where equilibrium is obtained after applying the initial pore pressure to the formation along with the initial in-situ stresses. The next step(s) simulates the HF stage(s), where a specific volume of fluid is injected along the perforations. In the proposed method, it is noted that the initial fractures or perforations are simulated by enriched elements, and the fracturing fluid flow is applied directly to the edge phantom nodes of the enriched elements. The geologic parameters and the material properties are represented in Table 1 (Shojaei et al., 2014; Sobhaniaragh et al., 2016b). In-situ stresses in the x, y, and z directions, are taken to be -19.0 MPa, -20.5 MPa and -19.0 MPa, respectively, unless otherwise stated.

4. Numerical Results and Discussion

4.1. Validation of Numerical Simulation

In order to validate the numerical simulation, the results obtained for an individual hydraulically fluid-driven fracture are compared with the analytical solution developed by Geertsma et al. (1969); Khristianovic and Zheltov (1955), termed the KGD model. This model is valid for a plane strain condition in the horizontal plane, with a purely viscous fluid in the laminar flow regime, and a constant injection rate along the wellbore. In addition, there is no leak-off into the formation in this model. In order to mitigate the unrealistic stress singularity ahead of the crack, zipper cracks introduced by Valk and Economides (1995) provided a mild crack tip closure by virtue of a negative pressure dispersion in the vicinity of the crack tip within the un-wetted zone, or cohesive zone. In a limiting approach, by assuming that the dry zone in front of the crack tip is small, the shape of the wet zone in the crack can be approximated by an ellipse with the width at location x identical to $\left(4E\hat{P}\Big/(1-\nu^2)\right)\sqrt{{x_c}^2-x^2}$ where $\hat{P}$ denotes the constant fluid pressure within the crack, x_c denotes the crack half-length, E is the modulus of elasticity and ν is Poisson's ratio. The Crack Mouth Pressure (CMP), Crack Mouth Opening Displacement (CMOD), and crack half-length (x_c) are expressed as (Valk and Economides, 1995)

$$\mathrm{CMP} = S_{h,\min} + 1.09\left(\frac{E^2\mu}{(1-\nu^2)^2}\right)^{1/3} t^{-1/3} \tag{23}$$

$$\mathrm{CMOD} = 2.36\left(\frac{\mu Q^3(1-\nu^2)}{Eh^3}\right)^{1/6} t^{1/3} \tag{24}$$

$$x_c = 0.539\left(\frac{EQ^3}{(1-\nu^2)h^3}\right)^{1/6} t^{2/3} \tag{25}$$

where Q is the total injection rate, h denotes the crack height, μ is the viscosity of the fluid, and $S_{h,\min}$ is the minimum horizontal stress. The numerical results obtained by CPNM for CMP, fracture aperture profile, and CMOD depicted in Figs. 7-9, respectively, are compared with the analytical solution. From Figs. 7-9, one can see that excellent agreement exists between the results of the present method and those obtained by the KGD model.

In order to verify the present methodology, which considers the stress shadowing effect in the propagation of multiple fractures, it is compared against the Displacement Discontinuity Method (DDM) (Sesetty et al., 2015) in simulating the propagation of double fluid-driven fractures. In Ref. (Sesetty et al., 2015), the model was based on 2-D plane strain and the DDM was used to predict fracture deformation and propagation. In addition, no fluid leak-off into the formation was considered and the fracture propagation direction was driven by the maximum principal tensile stress criterion. The FS between two fractures was set as 9m (30 ft.) and the fractures were stimulated sequentially. Fig. 10 compares the fracture geometries of the first and second stages created along the horizontal wellbore by using the DDM and CPNM. In this figure, the discrepancy between the geometries of the first and second fractures is attributed to the stress shadowing effect. Fig. 10 demonstrates a good agreement between fracture geometries obtained by the DDM and those by the CPNM.

4.2. Parametric investigations

In this section, we consider the effects of stress shadowing in the MZF completion design. Specifically, by conducting a large number of simulation runs, we study the effects on the stress anisotropy, pore pressure, leak-off flow rate. One of the main contributions of the present work is to shed light on the zone around the induced fractures in which the stress is altered, and how this is affected by FS. In particular, in this section we evaluate the horizontal stress contrast in the area near the fracture tip, contrary to (Roussel et al., 2011; Manchanda et al., 2014) in which only the point of the fracture initiation along the wellbore is considered.

4.2.1. Pore pressure of the porous formation

Pore pressure contours in the formation for the case of an MZF design with FS=18 m and FS=31 m are shown in Figs. 11a and 11b. In this example, the fracturing fluid is injected into the first perforation on Well No. 1 for a period of 60 minutes, and at the end of this stage fracture number 1 (Fr. #1) is created. Then, the second perforation on Well No. 1 is fractured, and this is followed by the first stage on Well No. 2. It should be noted that FS used in this section denotes the spacing between the first and second perforation on Well No. 1. Also, according to MZF, the perforation created on Well No. 2 is situated midway between the first and second perforations on Well No. 1. It is evident from Fig. 11a that the length of Fr. #1 is divided into $L_{f_{1,1}}$ and $L_{f_{1,2}}$.

This is because after terminating the first stage on Well No. 1 and creating $L_{f_{1,1}}$, the second stage starts and Fr. #2 propagates, altering the local stresses between Fr. #1 and Fr. #2 and imposing forces on the surface of Fr. #1. Accordingly, the fracturing fluid in Fr. #1 plays a role as a driving force so that $L_{f_{1,2}}$ is created as the Fr. #2 propagates. It is worth noting that the length of $L_{f_{1,2}}$ is considerably smaller than that of Fig. 11b owing to the larger FS and, as a result, there are reduced stress shadow effects. Under closer inspection, it can be seen that Fr. #3 first propagates in the direction of maximum in-situ horizontal stress, and afterwards it reorients itself in the direction of the local maximum horizontal stress induced by the stress shadow effects of other fractures. Also observed from Figs. 11a and 11b is that by choosing FS=18 m, the Fr. #1 on Well No. 1 grows in a straight path whereas by selecting FS=31 m, the Fr. #3 on Well No. 2 propagates straight towards the area in the middle of two other fractures. This point will be further discussed in the following.

4.2.2. Stress anisotropy

Fig. 12 demonstrates the variation in the horizontal stress contrast ($\sigma_{H,\max} - \sigma_{h,\min}$) along the wellbore with perpendicular distance from the fracture in the first stage for various fracture lengths, L_{f_1}, and several distances (L_i^1) from the the horizontal wellbore No. 1. It should be noted that the horizontal stress contrast presented in this figure has been obtained after terminating the first stage and before staring the second stage, i.e. using the same strategy as (Manchanda et al., 2014; Roussel et al., 2011). It can be inferred from Fig. 12 that by increasing the fracture length, the region of low stress contrast due to stress shadowing effects moves away from the fracture. In addition, it can be seen that for the case with the same fracture length, the horizontal stress contrast decreases with increasing distance form the horizontal wellbore, which implies that the region of low horizontal stress contrast is deviated from the first fracture owing to the stress shadow effect.

Fig. 13 shows the variation in the horizontal stress contrast in the direction perpendicular to the first fracture for FS=18 m and FS=31 m. In these results, the horizontal stress contrast is shown for three specific distances (L_1^1 = 6 m, L_2^1 = 12 m, and L_3^1 = 12 m) from Well No. 1 when the fracture tip approaches those distances. Fig. 12 shows a different behaviour in the results obtained after terminating the first stage. Several simulation runs have been conducted in this research, and eventually it has been concluded that with FS of 18 m in the MZF scenario, the second fracture is not deviated from the first fracture, and follows a straight propagation path owing to a low horizontal stress gradient, as depicted in Fig. 13. Further, the horizontal stress contrast significantly decreases in the area near the fracture tip by decreasing the FS, while the overall horizontal stress contrast between fractures is considerably lower for the cases with larger FS. It is worth noting that the reduction in horizontal stress contrast as a result of stress shadowing plays an important role in opening the natural fractures and eventually increasing the fracture complexity (Dahi Taleghani et al., 2013; Soliman et al., 2010). Refs. (Manchanda et al., 2014; Roussel et al., 2011) concluded that in a region of low stress contrast, in particular in the middle of two fractures, there is a high probability that an induced fracture will propagate along a straight path transversely and tap into a pre-existing fracture network. In contrast, a comparison of Figs. 12 and 13 reveals that a new fracture growing into the altered-stress region has the capability to alter the local stresses.

The direction of maximum horizontal stress in the area between two horizontal wellbores is depicted in Fig. 14a. Based on several simulation results conducted in this study, the stress-altered zones, which have an effect on the second stage on Well. No. 1, are divided into attraction and repulsion zones. If the second stage started in the attraction zone, the Fr. #2 would follow a non-planar crack path due to the stress shadowing effect caused by Fr. #1, as shown in Fig. 14b. It is interesting to note that after completing the first stage, the direction of the second induced fracture

cannot be estimated only by considering the direction of the maximum horizontal stress. This is because the propagation of the second fracture alters the existing local stress and imposes new stress shadowing conditions in the area, changing its propagation path. By increasing the FS to the critical value of 18 m, the Fr. #2 is not deviated and follows a straight propagation path while the Fr. #3 on Well No. 2, which is situated in the curving zone, follows a non-planar path. On the other hand, when the FS in the MZF design reaches a value of 31 m, in other words, the distance of Fr. #3 on Well No. 2 attains a value of 15.5 m from the Fr. #1, Fr. #3 exhibits an unchanged crack path as shown in Fig. 14c. In addition, by increasing the FS from the critical value of 18 m, the Fr. #2 is located in the repulsion zone, which implies that it is deviated from the first fracture, although the degree of deviation decreases by moving away from the Fr. #1. Furthermore, the Fr. #3 on Well No 2 retains its straight propagation path moving away from the Fr. #1. We conclude that the stress-altered area near Well No. 2 comprises two specific zones, including curving and unaltered zones.

4.2.3. In-plane shear stress

Figs. 15a-15d show the effect of the propagation of the Fr. #3 into the area between two pre-existing fractures (Fr. #1 and Fr. #2) on the shear stress for the MZF design with various FS. The results obtained show that after creating the Fr. #2, the shear stress in the region between two fractures is suppressed owing to stress shadowing effects. As the Fr. #3 invades this area, it not only considerably alters the magnitude of shear stress, but it also causes far more of the reservoir to be exposed to some alteration in shear stress. Consequently, this promotes activation of any planes of weakness and natural fractures which exist in non-conventional reservoirs such as shale plays (Rezaei et al., 2015; Rafiee et al., 2012). As depicted in Figs. 15a-15d, the propagation of the Fr. #3 into the repulsion zone between Fr. #1 and Fr. #2 has a substantially greater effect on the shear stress than those located in the attraction zone. Importantly, growth of the third fracture from the offset wellbore can change the direction of the shear stress, thereby increasing the probability of activating pre-existing natural fractures and, as a result, promoting greater fracture complexity.

4.2.4. Leak-off flow rate

The variation in the leak-off flow rate in the cracked element adjacent to the wellbore, during the HF time of operation, is shown in Fig. 16. In this example, HF time for each stage is taken to be 4000 second. Specific observations apparent from Fig. 16 are as follows: (**i**) The leak-off flow rate becomes considerably larger as the HF job in MZF design proceeds to the subsequent stages; (**ii**) by increasing the FS in the repulsion zone, the leak-off flow rate in the second stage is reduced, although this observation is reversed in the third stage which is performed on the offset wellbore.

Acknowledgments

The authors would like to acknowledge the research support of CNPq (Conselho Nacional de Desenvolvimento Científico e Tecnológico) with grant number of 164774/2014-9, of FAPERJ (Fundação de Amparo a Pesquisa do Estado do Rio de Janeiro), and of ANP (Agência Nacional do Petróleo) through PETROBRAS network of applied geophysics with grant number of 0050.0070743.11.9.

Conclusion

A comprehensive study has been presented for the "Modified Zipper-Frac" (MZF) design using closely spaced fractures to enhance the complexity of the fracture network in the area between

two adjacent horizontal wellbores. Taking the stress shadowing effects into account, the Cohesive Segments Method, in combination with Phantom Node Method (CPNM), has been established to simulate the propagation of non-planar hydraulic fractures. In order to treat the filter cake as a pressure-dependent layer, Settari's fluid leak-off model was employed by means of a user-defined subroutine. A large number of numerical simulations using CPNM have been carried out to investigate several factors, such as the stress isotropy, the in-plane shear stresses, and the leak-off flow rate.

The results suggest that the stress-altered zones, which have an crucial effect on the second stage on Well No. 1, are divided into attraction and repulsion zones. On the other hand, the area near Well No. 1, where the third fracture propagates, is partitioned into curving and unaltered zones.

The simulation results show that as a third fracture from the offset wellbore propagates into the area between pre-existing fractures, not only does it considerably alter the magnitude of shear stresses, but it also causes far more of the reservoir to become exposed to some alteration in shear stress. Accordingly, this leads to activation of pre-existing planes of weakness and natural fractures in non-conventional reservoirs such as shale plays. This point also highlights the benefits of the MZF design in decreasing the magnitude of shear stresses through stress shadow effects.

The simulation results suggest that a new fracture growing into the altered-stress region has the capability to alter the local stresses and change the low-stress contrast region. In addition, the numerical results have revealed that the horizontal stress contrast significantly decreases in the area near the fracture tip when the fracture spacing is reduced, while overall horizontal stress contrast between fractures is considerably lower for the cases with larger fracture spacing. It has been also shown that the leak-off flow rate increases substantially as the hydraulic fracturing process in the MZF design proceeds to its later stages.

References

Adachi, J. I., 2001. Fluid-driven fracture in permeable rock. University of Minnesota, Minneapolis.

Areias, P., Belytschko, T., 2005. Analysis of three-dimensional crack initiation and propagation using the extended finite element method. International Journal for Numerical Methods in Engineering 63 (5), 760–788.

Baker, G., Karihaloo, B. L., 2004. Fracture of Brittle Disordered Materials: Concrete, Rock and Ceramics. CRC Press.

Belytschko, T., Ong, J., L, W., Kennedy, J., 1984. Hourglass control in linear and nonlinear problems. Computer Methods in Applied Mechanics and Engineering 43 (3), 251–276.

Benzeggagh, M., Kenane, M., 1996. Measurement of mixed-mode delamination fracture toughness of unidirectional glass/epoxy composites with mixed-mode bending apparatus. Composites science and technology 56 (4), 439–449.

Bunger, A. P., Detournay, E., Garagash, D. I., 2005. Toughness-dominated hydraulic fracture with leak-off. International journal of fracture 134 (2), 175–190.

Camacho, G. T., Ortiz, M., 1996. Computational modelling of impact damage in brittle materials. International Journal of solids and structures 33 (20), 2899–2938.

Carpinteri, A., 2012. Nonlinear crack models for nonmetallic materials. Vol. 71. Springer Science & Business Media.

Carter, R., 1957. Derivation of the general equation for estimating the extent of the fractured area. Appendix I of Optimum Fluid Characteristics for Fracture Extension, Drilling and Production Practice, GC Howard and CR Fast, New York, New York, USA, American Petroleum Institute, 261–269.

Charlez, P. A., 1997. Rock mechanics: petroleum applications. Vol. 2. Editions Technip.

Dahi Taleghani, A., Ahmadi, M., Olson, J., et al., 2013. Secondary fractures and their potential impacts on hydraulic fractures efficiency. In: ISRM International Conference for Effective and Sustainable Hydraulic Fracturing. International Society for Rock Mechanics.

Geertsma, J., De Klerk, F., et al., 1969. A rapid method of predicting width and extent of hydraulically induced fractures. Journal of Petroleum Technology 21 (12), 1–571.

Haddad, M., Sepehrnoori, K., 2015. Simulation of hydraulic fracturing in quasi-brittle shale formations using characterized cohesive layer: Stimulation controlling factors. Journal of Unconventional Oil and Gas Resources 9, 65–83.

Hansbo, A., Hansbo, P., 2004. A finite element method for the simulation of strong and weak discontinuities in solid mechanics. Computer methods in applied mechanics and engineering 193 (33), 3523–3540.

Hattori, G., Trevelyan, J., Augarde, C. E., Coombs, W. M., Aplin, A. C., 2017. Numerical simulation of fracking in shale rocks: current state and future approaches. Archives of Computational Methods in Engineering 24 (2), 281–317.

Hillerborg, A., 1985. The theoretical basis of a method to determine the fracture energyg f of concrete. Materials and structures 18 (4), 291–296.

Ingraffea, A. R., Heuz, F. E., Ko, H.-Y., Gerstle, K., et al., 1977. An analysis of discrete fracture propagation in rock loaded in compression. In: The 18th US Symposium on Rock Mechanics (USRMS). American Rock Mechanics Association.

Khoei, A., Mohammadnejad, T., 2011. Numerical modeling of multiphase fluid flow in deforming porous media: A comparison between two-and three-phase models for seismic analysis of earth and rockfill dams. Computers and Geotechnics 38 (2), 142–166.

Khristianovic, S., Zheltov, A., 1955. 3. formation of vertical fractures by means of highly viscous liquid. In: 4th World Petroleum Congress. World Petroleum Congress.

Kumar, D., Ghassemi, A., 2016. A three-dimensional analysis of simultaneous and sequential fracturing of horizontal wells. Journal of Petroleum Science and Engineering 146, 1006–1025.

Manchanda, R., Sharma, M. M., et al., 2014. Impact of completion design on fracture complexity in horizontal shale wells. SPE Drilling & Completion 29 (01), 78–87.

Meyer, B. R., Bazan, L. W., et al., 2011. A discrete fracture network model for hydraulically induced fractures-theory, parametric and case studies. In: SPE Hydraulic Fracturing Technology Conference. Society of Petroleum Engineers.

Nagel, N., Sheibani, F., Lee, B., Agharazi, A., Zhang, F., et al., 2014. Fully-coupled numerical evaluations of multiwell completion schemes: The critical role of in-situ pressure changes and well configuration. In: SPE Hydraulic Fracturing Technology Conference. Society of Petroleum Engineers.

Nagel, N., Zhang, F., Sanchez-Nagel, M., Lee, B., et al., 2013. Quantitative evaluation of completion techniques on influencing shale fracture complexity. In: ISRM International Conference for Effective and Sustainable Hydraulic Fracturing. International Society for Rock Mechanics.

Nagel, N. B., Gil, I., Sanchez-Nagel, M., Damjanac, B., et al., 2011. Simulating hydraulic fracturing in real fractured rocks-overcjavascript:overcoming the limits of pseudo3d models. In: SPE Hydraulic Fracturing Technology Conference. Society of Petroleum Engineers.

Needleman, A., 1987. A continuum model for void nucleation by inclusion debonding. Journal of applied mechanics 54 (3), 525–531.

Olsen, T. N., Bratton, T. R., Thiercelin, M. J., et al., 2009. Quantifying proppant transport for complex fractures in unconventional formations. In: SPE Hydraulic Fracturing Technology Conference. Society of Petroleum Engineers.

Olson, J. E., Taleghani, A. D., et al., 2009. Modeling simultaneous growth of multiple hydraulic fractures and their interaction with natural fractures. In: SPE Hydraulic Fracturing Technology Conference. Society of Petroleum Engineers.

Rabczuk, T., Zi, G., Gerstenberger, A., Wall, W., 2008. A new crack tip element for the phantom-node method with arbitrary cohesive cracks. International Journal for Numerical Methods in Engineering 75 (5), 577–599.

Rafiee, M., Soliman, M., Pirayesh, E., et al., 2012. Hydraulic fracturing design and optimization: a modification to zipper frac. In: SPE Annual Technical Conference and Exhibition. Society of Petroleum Engineers.

Rezaei, A., Rafiee, M., Soliman, M., Morse, S., et al., 2015. Investigation of sequential and simultaneous well completion in horizontal wells using a non-planar, fully coupled hydraulic fracture simulator. In: 49th US Rock Mechanics/Geomechanics Symposium. American Rock Mechanics Association.

Rios, A., Gutierrez, G., Nagel, N., Zhang, F., Sanchez-Nagel, M., Lee, B., et al., 2013. Stress shadow evaluations for chicontepec–evaluating new completion options. In: 47th US Rock Mechanics/Geomechanics Symposium. American Rock Mechanics Association.

Roussel, N. P., Sharma, M. M., et al., 2010. Quantifying transient effects in altered-stress refracturing of vertical wells. SPE Journal 15 (03), 770–782.

Roussel, N. P., Sharma, M. M., et al., 2011. Strategies to minimize frac spacing and stimulate natural fractures in horizontal completions. In: SPE Annual Technical Conference and Exhibition. Society of Petroleum Engineers.

Sesetty, V., Ghassemi, A., et al., 2015. Simulation of simultaneous and zipper fractures in shale formations. In: 49th US Rock Mechanics/Geomechanics Symposium. American Rock Mechanics Association.

Sethian, J., 1999. Level set methods and fast marching methods: evolving interfaces in computational geometry, fluid mechanics, computer vision, and materials science. Vol. 3. Cambridge university press.

Settari, A., Price, H., et al., 1984. Simulation of hydraulic fracturing in low-permeability reservoirs. Society of Petroleum Engineers Journal 24 (02), 141–152.

Shojaei, A., Dahi-Taleghani, A., Li, G., 2014. A continuum damage failure model for hydraulic fracturing of porous rocks. International Journal of Plasticity 59, 199–212.

Sih, G., 1973. Some basic problems in fracture mechanics and new concepts. Engineering fracture mechanics 5 (2), 365–377.

Sobhaniaragh, B., Mansur, W., Peters, F., 2016a. On the stress-shadow effects of multiple-stage hydraulic fracturing in unconventional reservoirs by using cohesive phantom node method. In: SEG Technical Program Expanded Abstracts 2016. Society of Exploration Geophysicists, pp. 3422–3427.

Sobhaniaragh, B., Mansur, W., Peters, F., 2016b. Three-dimensional investigation of multiple stage hydraulic fracturing in unconventional reservoirs. Journal of Petroleum Science and Engineering 146, 1063–1078.

Soliman, M., East, L., Augustine, J., et al., 2010. Fracturing design aimed at enhancing fracture complexity. In: SPE EUROPEC/EAGE Annual Conference and Exhibition. Society of Petroleum Engineers.

Stevens, P., 2012. The shale gas revolution: Developments and changes. Chatham House, 2–3.

Terzaghi, K., 1951. Theoretical soil mechanics. Chapman And Hall, Limited.; London.

Tvergaard, V., Hutchinson, J. W., 1992. The relation between crack growth resistance and fracture process parameters in elastic-plastic solids. Journal of the Mechanics and Physics of Solids 40 (6), 1377–1397.

Valk, P., Economides, M., 1995. Hydraulic fracture mechanics. Wiley, New York.

Vermeer, P., Verruijt, A., 1981. An accuracy condition for consolidation by finite elements. International Journal for numerical and analytical methods in geomechanics 5 (1), 1–14.

Vermylen, J., Zoback, M., et al., 2011. Hydraulic fracturing, microseismic magnitudes, and stress evolution in the barnett shale, texas, usa. In: SPE Hydraulic Fracturing Technology Conference. Society of Petroleum Engineers.

Weng, X., Siebrits, E., et al., 2007. Effect of production-induced stress field on refracture propagation and pressure response. In: SPE Hydraulic Fracturing Technology Conference. Society of Petroleum Engineers.

Winegarden, W., 2016. Regulating the upstream energy industry.

Wu, H., Pollard, D. D., 2002. Imaging 3-d fracture networks around boreholes. AAPG bulletin 86 (4), 593–604.

Wu, R., Kresse, O., Weng, X., Cohen, C.-E., Gu, H., et al., 2012. Modeling of interaction of hydraulic fractures in complex fracture networks. In: SPE Hydraulic Fracturing Technology Conference. Society of Petroleum Engineers.

Zienkiewicz, O., Shiomi, T., 1984. Dynamic behaviour of saturated porous media; the generalized biot formulation and its numerical solution. International journal for numerical and analytical methods in geomechanics 8 (1), 71–96.

Zimmerman, R. W., Bodvarsson, G. S., 1996. Hydraulic conductivity of rock fractures. Transport in porous media 23 (1), 1–30.

Appendix A.

The essential boundary conditions prescribed on the external boundaries are described by

$$\begin{aligned} \mathbf{u} &= \bar{\mathbf{u}} \quad \text{on} \quad \Gamma_u \\ p &= \bar{p} \quad \text{on} \quad \Gamma_p \end{aligned} \tag{A.1}$$

and the natural boundary conditions imposed on the boundaries of the body are as follows

$$\dot{\mathbf{q}}_t . \mathbf{n}_\Gamma = \bar{q}_w \quad \text{on} \quad \Gamma_{in} \tag{A.2}$$

where $\bar{q}_w$ is the flow rate of the fracturing fluid imposed on the perforation Γ_{in}, and $\mathbf{n}_\Gamma$ denotes the unit outward normal vector to the external boundary. In addition, the following boundary conditions on the surfaces of the crack are prescribed

$$\begin{aligned} \boldsymbol{\sigma} . \mathbf{n}_{\Gamma_d} &= \mathbf{t}_d - p\mathbf{n}_{\Gamma_d} \\ \left[\!\left[\mathbf{v}_f \right]\!\right] . \mathbf{n}_{\Gamma_d} &= q_{wd} \end{aligned} \tag{A.3}$$

where $\mathbf{t}_d$ denotes the cohesive traction acting in the FPZ, q_{wd} is the flux of the fluid leak-off along the fracture toward the surrounding formation, and $\mathbf{n}_{\Gamma_d}$ is the unit normal vector to the crack. The notation $[\![]\!]$ represents the discrepancy between the corresponding values at the two crack faces.

In order to derive the weak form of the governing equations, we integrate the equilibrium equation (Eq. 8) and continuity equation for the fluid flow (Eq. 9) with admissible test functions over the analyzed domain. Employing the divergence theorem, imposing the natural boundary conditions, and satisfying the boundary conditions on the crack faces, the weak form of the equilibrium equation is found to be

$$\int_\Omega \nabla^s \boldsymbol{\eta} : \boldsymbol{\sigma} d\Omega + \int_{\Gamma_d} [\![\boldsymbol{\eta}]\!] . (\mathbf{t}_d - p\mathbf{n}_{\Gamma_d}) d\Gamma = 0 \tag{A.4}$$

where ∇^s is the symmetric part of the gradient operator. This expression must hold for any admissible test function for the displacement field. It should be noted that the total stress $\boldsymbol{\sigma}$ in the integral Eq. A.4 must be replaced by the effective stress in Eq. 7. The weak form of the continuity equation of fluid flow within the porous medium is given by

$$\int_\Omega \zeta \frac{1}{Q} \dot{p} d\Omega + \int_\Omega \zeta \alpha \nabla . \dot{\mathbf{u}} d\Omega + \int_\Omega \frac{k}{\mu} \nabla \zeta . \nabla p d\Omega - \int_{\Gamma_d} \zeta q_{wd} d\Gamma = - \int_{\Gamma_{in}} \zeta \bar{q}_w d\Gamma \tag{A.5}$$

which must hold for any admissible test function for the fluid pressure field ζ. The weak form of the Eq. 2 is determined in a similar manner. Afterwards, the weak forms of the equilibrium and continuity equations are rendered in a discrete form by employing the CPNM formulations presented in Eqs. 20 and 21. Finally, the resultant equations representing coupled processes in the HF problem are required to be solved simultaneously. In the transient coupled pore pressure-effective stress analysis, the backward Euler formula (sometimes also referred to as the modified Crank-Nicolson operator), which provides unconditional stability, is used to integrate the continuity equation in time. Generally, solutions for hydraulically fluid-driven fractures are rigorous to establish even for simple geometries. This difficulty comes from moving boundary conditions, and non-linearity of the governing equation for fluid flow in fractures. Non-linearity is attributed to the fact that fracture permeability is correlated to fracture width with a cubic function. The system of non-linear equations is solved numerically by an incremental-iterative solution, based on the Newton-Raphson technique. The integration procedure for consolidation analysis is reinforced by a minimum time step criterion proposed by Vermeer and Verruijt (1981) to avoid spurious oscillations which may occur in the solution. This criterion introduces a correlation between the minimum allowable time increment and the element size as follows

$$\Delta t \geq \frac{\gamma_F}{6\,E\,k}(\Delta h)^2 \tag{A.6}$$

where γ_F is the specific weight of fluid, k is the permeability of the porous medium, E is the elastic modulus of the soil skeleton, Δt is the time increment, and Δh is a typical element dimension.

Table 1: Parameters for the hydraulic fracturing model.

Properties	Value
Elastic modulus of formation	1.294 MPa
Poissons ratio	0.25
Fluid viscosity	1 cp
Critical fracture energy	28 kN/m
Damage Initiation Stress of barrier layers	0.36 MPa
Damage Initiation Stress of pay zone	0.32 MPa
Formation effective permeability	4.9346165e-19 m^2
Specific weight of fluid	9.8 kN/m^3
Initial pore pressure	795 kPa
Pressure dependent leak-off coefficient	5.879e-10 $m^3/kPa.s$
Porosity	0.2
Injection rate per unit reservoir thickness	1.5e-3 m^3/s

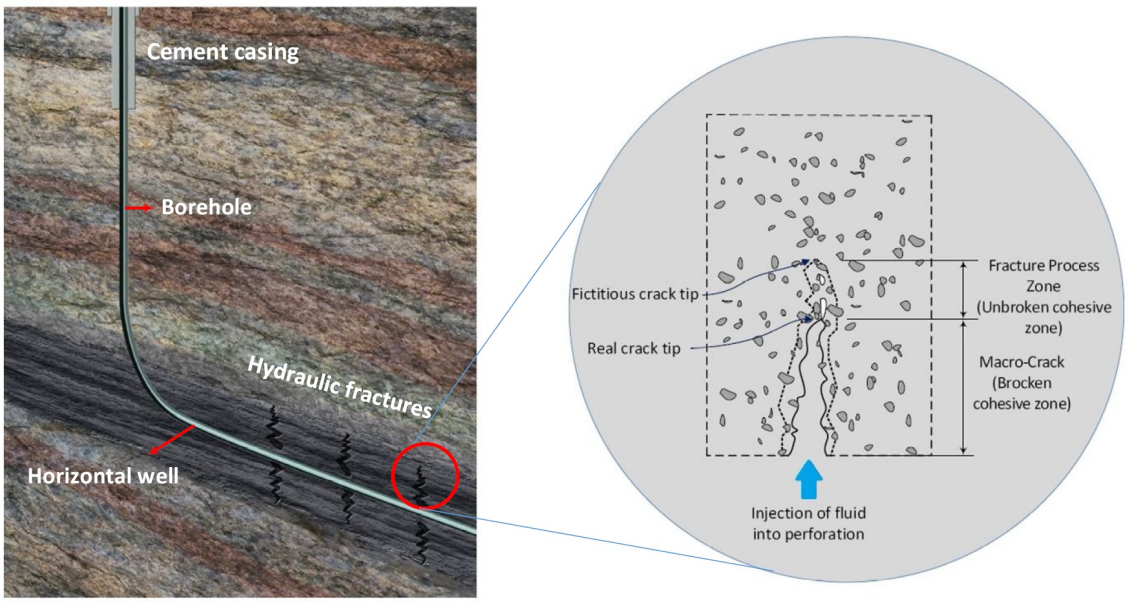

Figure 1: Schematic plot of hydraulic fracturing and embedded cohesive crack in a porous medium.

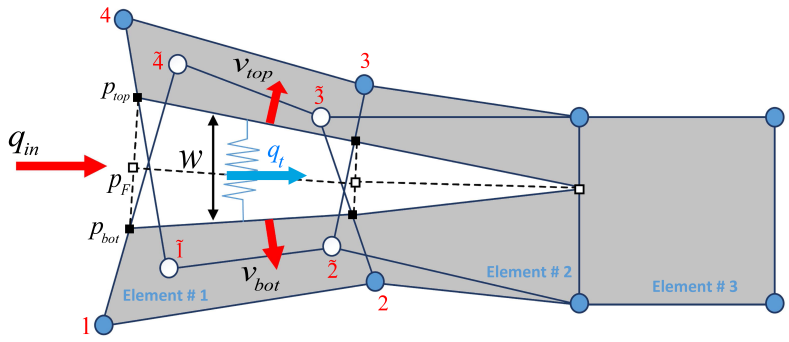

Figure 2: Model of fracturing fluid flow.

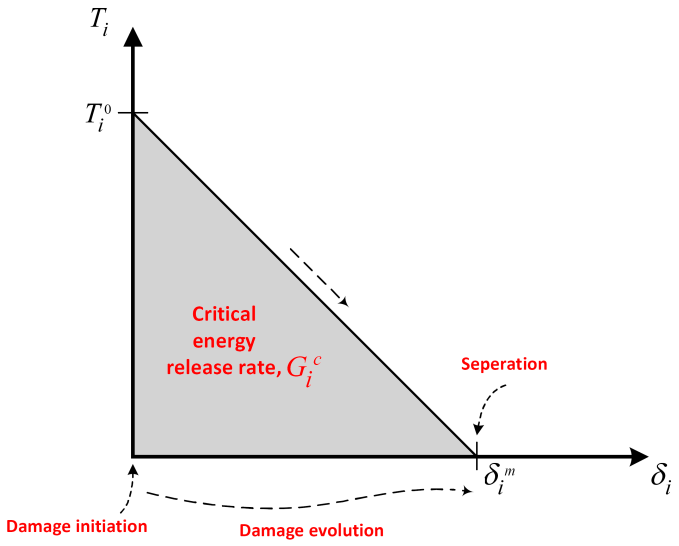

Figure 3: Cohesive traction-separation law with linear damage evolution.

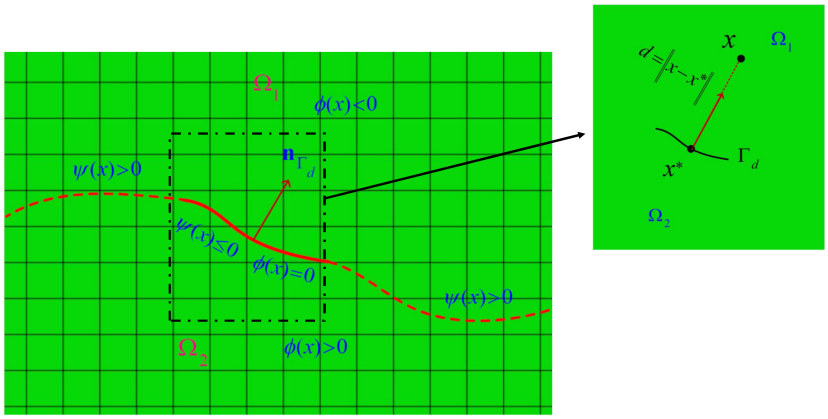

Figure 4: Illustration of a non-planar crack by two signed distance functions.

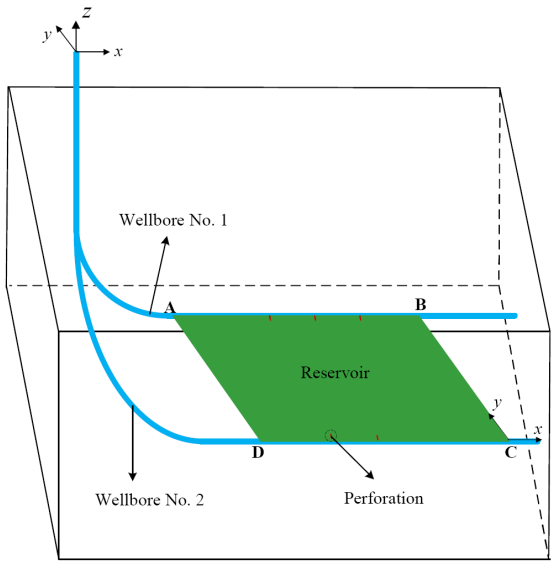

Figure 5: Three-dimensional configuration of the two lateral horizontal wellbores.

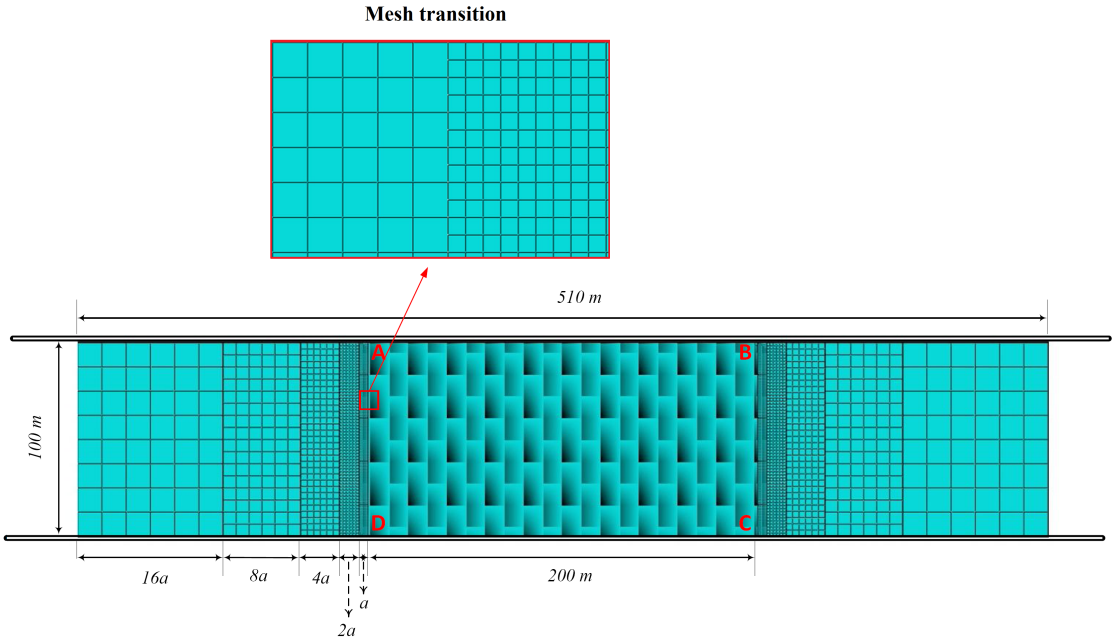

Figure 6: Finite element domain of modeled reservoir for the case of HF from two lateral wellbores (a= 5 m).

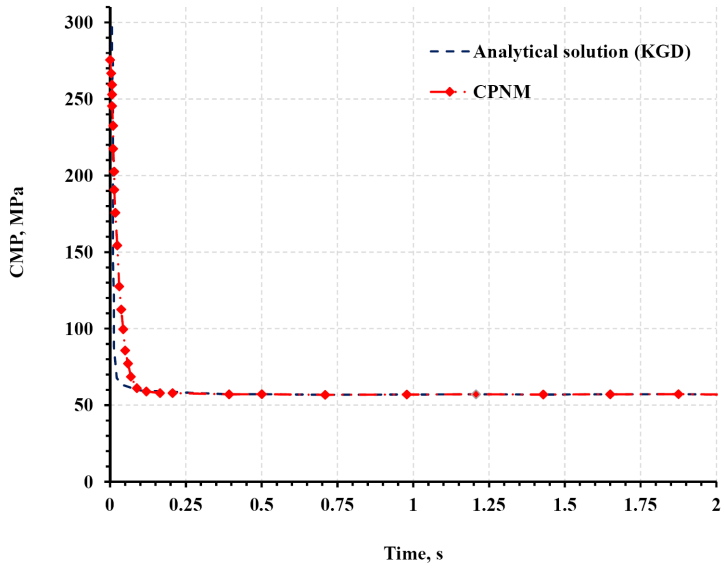

Figure 7: Comparison of CMP obtained by CPNM and analytical solution (KGD).

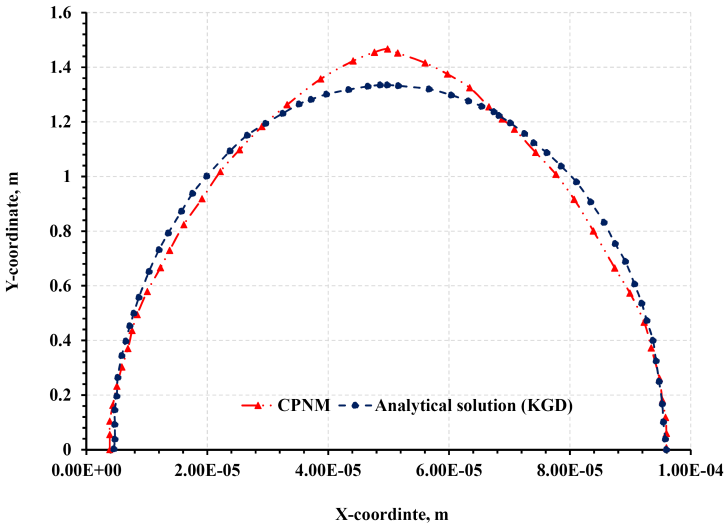

Figure 8: Comparison of fracture aperture profile obtained by CPNM and analytical solution (KGD).

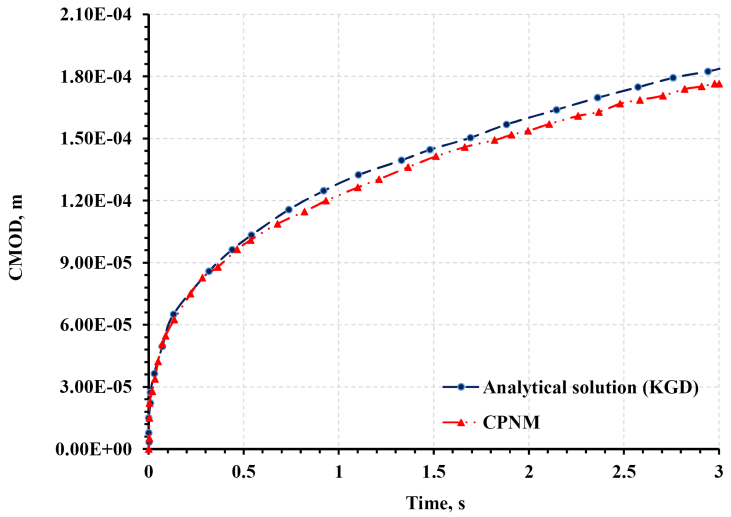

Figure 9: Comparison of CMOD obtained by CPNM and analytical solution (KGD).

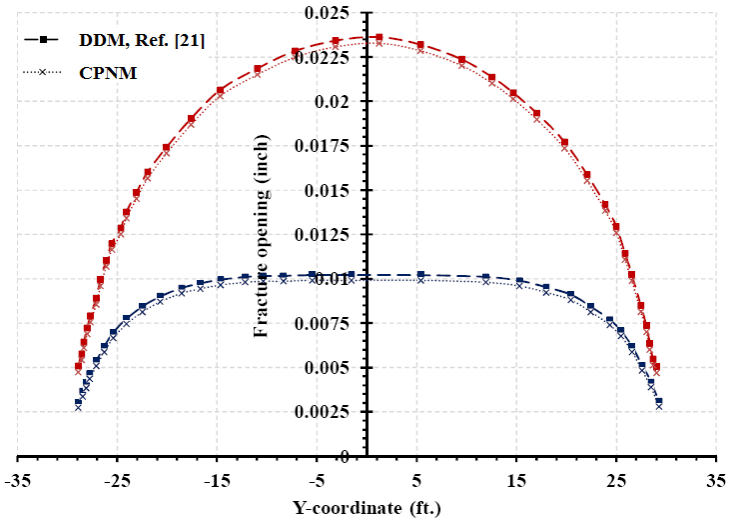

Figure 10: Comparison of fracture geometries of multiple fractures by using DDM model (Sesetty et al., 2015) and present CPNM (Injection rate=0.03 m^3/s, Fluid viscosity=1 cp), The red line denotes the first fracturing stage and the blue line represents the second fracturing stage.

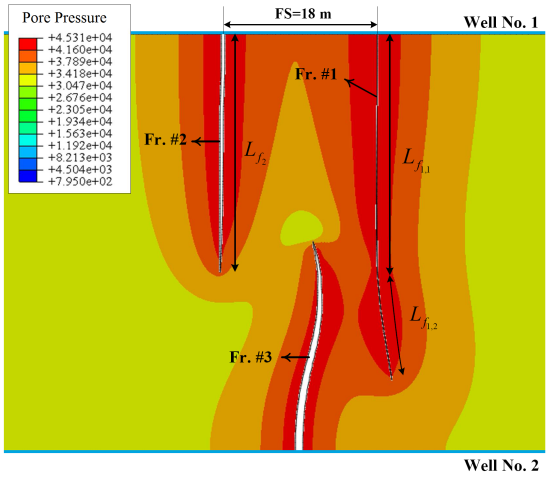

(a)

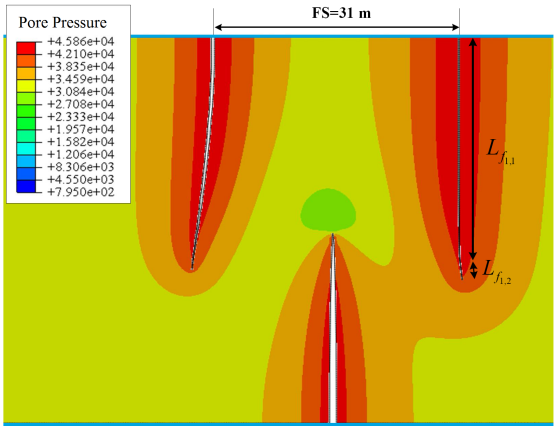

(b)

Figure 11: Pore pressure contours of the formation for the case of MZF design with: **a)** FS=18 m and **b)** FS=31 m.

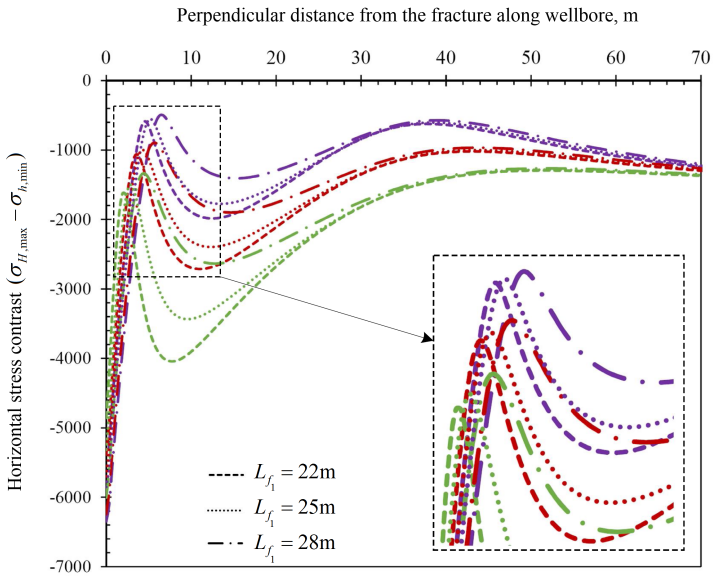

Figure 12: Variation in horizontal-stress contrast along the wellbore with perpendicular distance from Fr. #1 before starting the second stage. Green lines: $L_1^1 = 6$ m, Red lines: $L_2^1 = 12$ m, Violet lines: $L_3^1 = 18$ m.

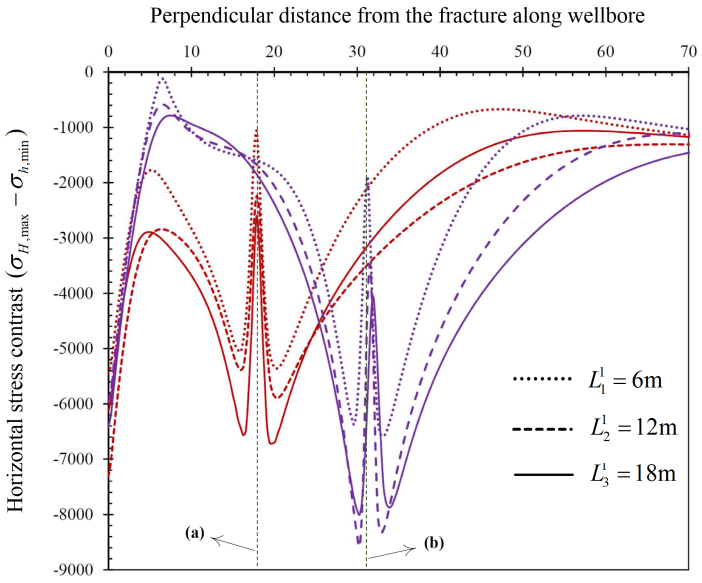

Figure 13: Illustration of variation in horizontal-stress contrast in the direction perpendicular to Fr. #1 for **a)** FS=18 m and **b)** FS=31 m.

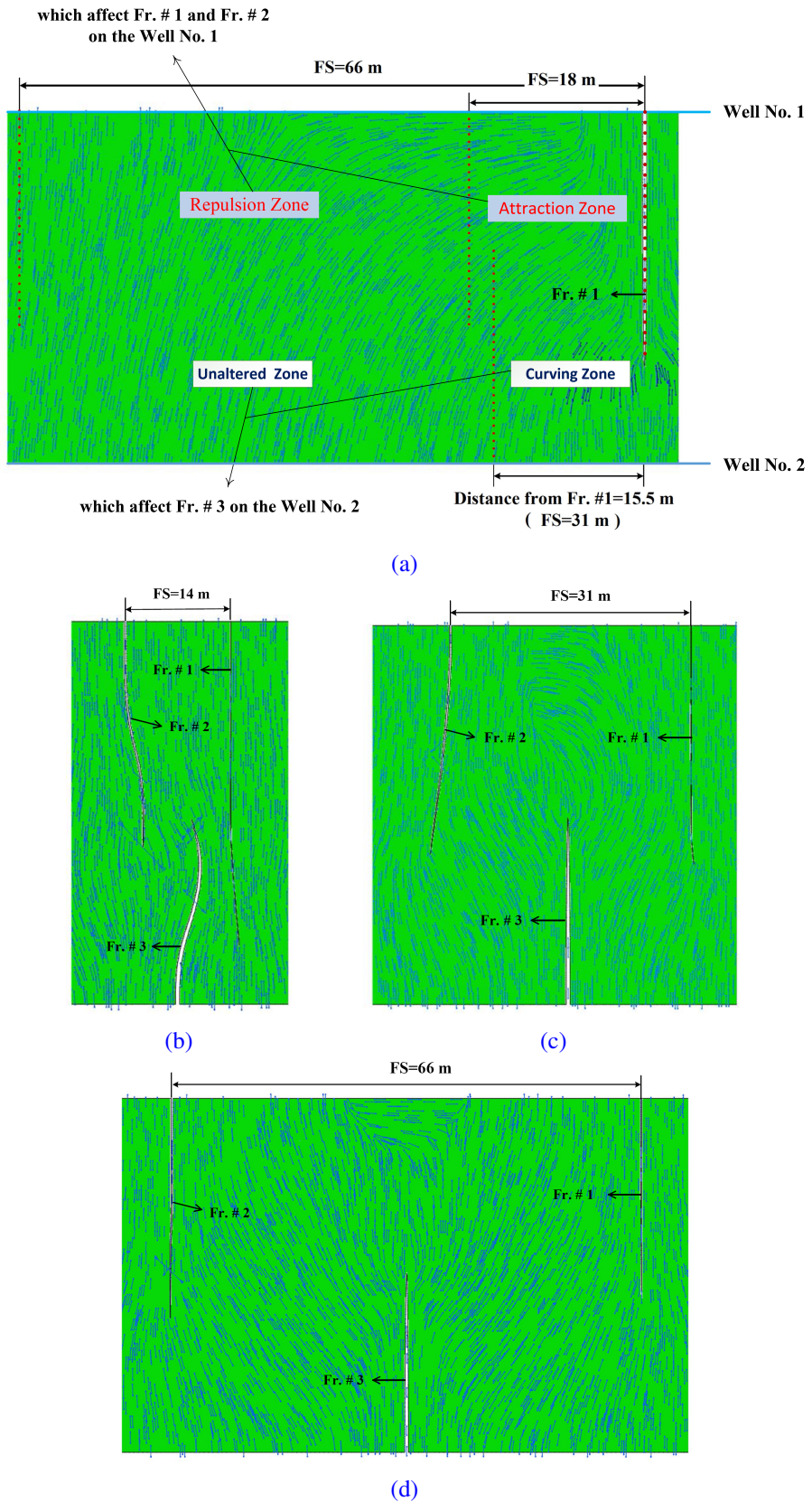

Figure 14: Direction of maximum horizontal stress in the area between two horizontal wellbores: **a)** Illustration of various zones after creating Fr. #1. **b)** MZF design with FS= 14 m in which Fr. #23 is located in the attraction zone whereas Fr. #2 is in the curving zone. **c)** MZF design with FS= 31 m in which Fr. #2 is located in the repulsion zone while Fr. #3 propagates in a straight path. **d)** MZF design with FS= 66 m in which Fr. #2 and Fr. #3 grow straight.

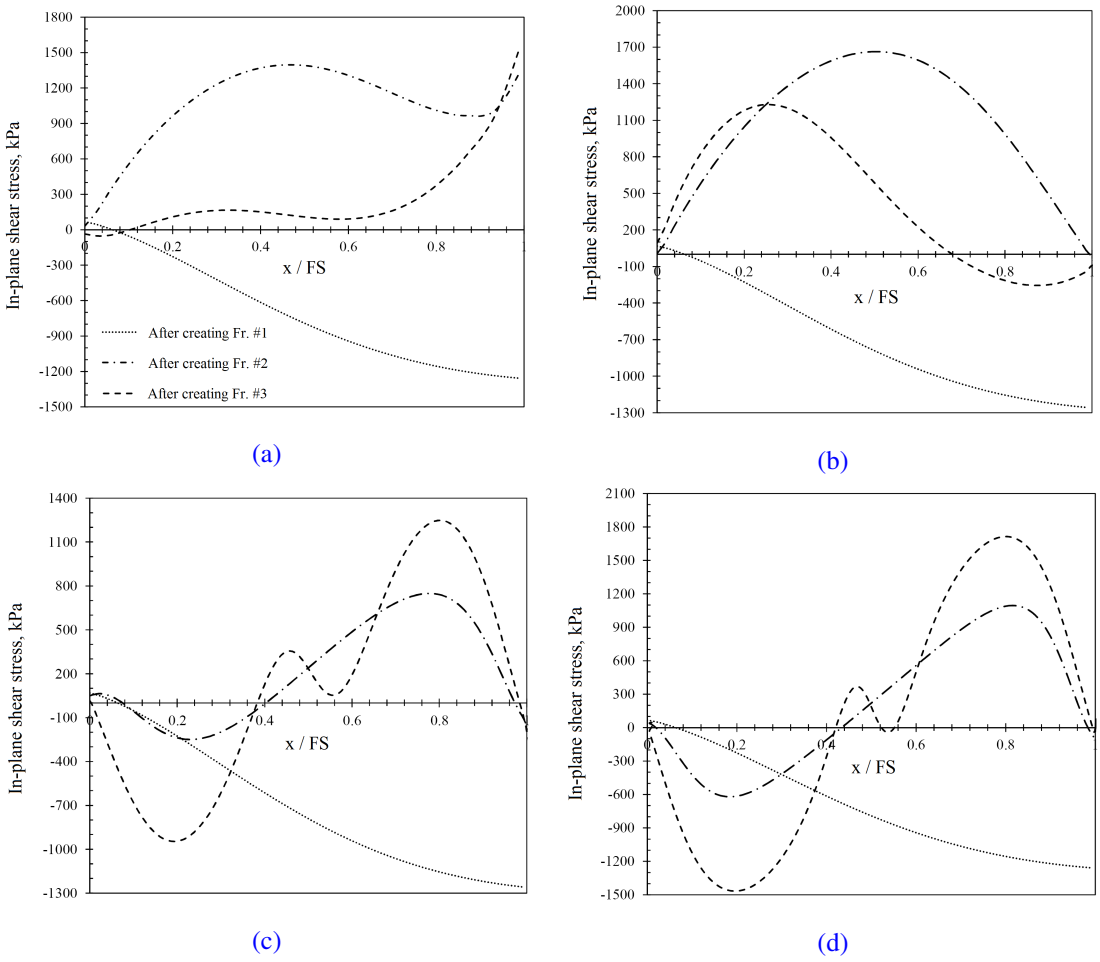

Figure 15: Distribution of in-plane shear stress along the horizontal wellbore with perpendicular distance from Fr. #1 (L^1 = 18 m) for MZF design with: **a)** FS=14 m. **b)** FS=18 m. **c)** FS=50 m. **d)** FS=66 m.

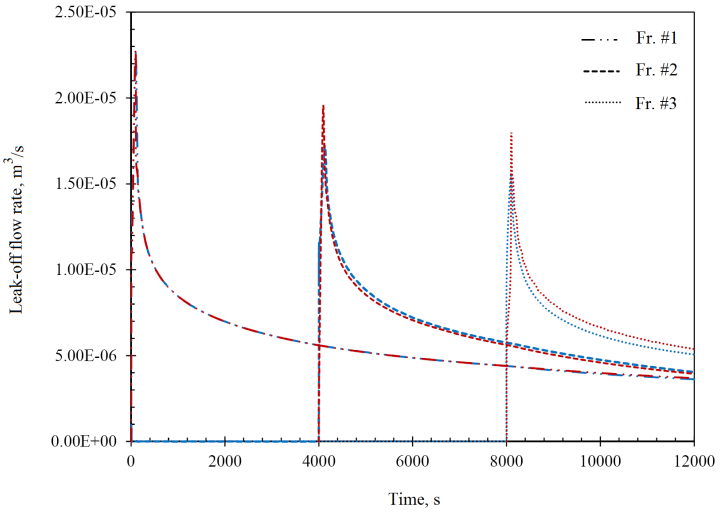

Figure 16: Variation of the leak-off flow rate in injection time for three fracturing stages; Blue line corresponds to FS=31 m, and red line denotes FS= 66 m.